Applications of Magnetic Resonance in Model Systems: Tumor Biology and Physiology[1]

Robert J. Gillies*, Zaver M. Bhujwalla[†], Jeffrey Evelhoch[‡], Michael Garwood[§], Michal Neeman[¶], Simon P. Robinson[#], Christopher H. Sotak[**] and Boudewijn Van Der Sanden[††]

*Department of Biochemistry, Arizona Cancer Center, University of Arizona, Tucson, AZ; [†]Oncology Section, Division of MR Research, Department of Radiology, The Johns Hopkins University School of Medicine, Baltimore, MD; [‡]MR Center, Harper Hospital, Wayne St. Univ., Detroit, MI; [§]Center for Magnetic Resonance Research, University of Minnesota School of Medicine, Minneapolis, MN; [¶]Department of Biological Regulation, The Weizmann Institute of Science, Rehovot 76100, Israel; [#]CRC Biomedical Magnetic Resonance Research Group, Department of Biochemistry and Immunology, St. George's Hospital Medical School, London, UK SW17 ORE ; **Department of Biomedical Engineering, Worcester Polytechnic Institute, Worcester, MA and Department of Radiology, University of Massachusetts Medical School, Worcester, MA and [††]Department of Radiology, Academic Hospital, Nijmegen, Netherlands

Abstract

A solid tumor presents a unique challenge as a system in which the dynamics of the relationship between vascularization, the physiological environment and metabolism are continually changing with growth and following treatment. Magnetic resonance imaging (MRI) and magnetic resonance spectroscopy (MRS) studies have demonstrated quantifiable linkages between the physiological environment, angiogenesis, vascularization and metabolism of tumors. The dynamics between these parameters continually change with tumor aggressiveness, tumor growth and during therapy and each of these can be monitored longitudinally, quantitatively and non-invasively with MRI and MRS. An important aspect of MRI and MRS studies is that techniques and findings are easily translated between systems. Hence, pre-clinical studies using cultured cells or experimental animals have a high connectivity to potential clinical utility. In the following review, leaders in the field of MR studies of basic tumor physiology using pre-clinical models have contributed individual sections according to their expertise and outlook. The following review is a cogent and timely overview of the current capabilities and state-of-the-art of MRI and MRS as applied to experimental cancers. A companion review deals with the application of MR methods to anticancer therapy. *Neoplasia* (2000) **2,** 139–151.

Introduction

A clear finding from magnetic resonance (MR) investigations into clinical and experimental tumors is that they are internally heterogeneous in terms of their perfusion, oxyge-nation and metabolism. This phenotype has a direct impact on the ability to cure cancers, since therapies that work in one volume of the tumor may not be effective in other volumes. The companion review (Evelhoch *et al.*, this volume) describes the use of MR to assess and improve therapeutic efficacy. The current review describes research aimed at defining the causes of this heterogeneous physiology. No comparisons are made to other methods (e.g., microelectrodes for pH or oxygen, Doppler ultrasound or nuclear medicine for perfusion). MR is able to observe many diverse aspects of tumor physiology, often simultaneously or in the same exam. Because of this, it is a peerless technology.

Perfusion and Angiogenesis

Insights into Tumor Perfusion from MR Studies

Of the myriad facets that cancer displays, its ability to establish a vascular network is one of the most dangerous. This vascular network provides cancer cells with nutrients and oxygen to grow, as well as avenues to escape from. Paradoxically, it is also the primary means through which anti-neoplastic agents can be delivered to treat solid tumors. Interest in tumor vasculature has existed since the 1920s and before [1], and it was recognized as early as 1945 that malignant cells provoked a continuous vascular proliferation [2]. The earliest indirect evidence of the existence of

radioresistant hypoxic cells [3] in solid tumors came from observations made by Thomlinson and Gray on human specimens of bronchogenic carcinoma in 1955 [4]. Necrosis was found to occur at a distance of 160 μm or greater from the nearest vessel in the histologic sections. This distance corresponded closely to the diffusion distance calculated by them where the concentration of oxygen would approach zero.

Numerous studies, which now span almost a century (see Ref. [5] for review), have identified several features which are characteristic of tumor vasculature. Amongst these are i) spatial heterogeneity and chaotic structures, ii) arterio-venous shunts, iii) acutely collapsed vessels and transiently collapsing vessels, iv) poorly differentiated, fragile and leaky vessels lacking in smooth muscle cell lining, and v) vasculature which is frequently unable to match the rapid growth of cancer cells, resulting in areas of hypoxia and necrosis. Interest in tumor vascularization and angiogenesis has increased recently due to two findings. One is that high vascular density in histologic specimens may be predictive of the disposition of the tumor to metastasize [6,7]. The second finding is that repeated treatment cycles with the angiogenesis inhibitor, endostatin, induced tumor dormancy in experimental tumor models without inducing tumor drug resistance [8].

Neovascularization is essential for tumor growth and progression [9]. Tumor cells induce neovascularization through the release of angiogenesis factors and several factors have now been identified as angiogenic promoters and angiogenic inhibitors [9,10]. An angiogenic factor which appears to be most responsive to the abnormal physiological environments of hypoxia, extracellular acidosis and substrate deprivation occurring in solid tumors [11] is vascular endothelial growth factor (VEGF). VEGF induces angiogenesis [12–14] and is also a potent vascular permeability factor [15]. Angiogenesis continues to occur through the lifetime of the tumor since new vasculature has to be continually generated with tumor growth. Three quantities, tumor blood flow, tumor vascular volume and vascular permeability, have mainly been used to characterize tumor vasculature. Relative to the time frame of non-MR methods of studying vasculature, MR is very recent. However, both magnetic resonance imaging (MRI) and magnetic resonance spectroscopy (MRS) have provided unique and novel insights into tumor vasculature and the interaction between the vasculature and physiology and metabolism.

MRI of Tumor Vasculature

Vascularization can be evaluated with MRI using intrinsic endogenous contrast [16] or with exogenous paramagnetic contrast agents. The theoretical basis and applications of these methods to studying solid tumor vasculature has been recently reviewed [17]. Gadolinium chelates are the contrast agents most frequently used for MRI. When the ion is placed in a magnetic field, the seven unpaired electrons of gadolinium produce a large magnetic moment that results in paramagnetic properties, creating contrast in an MR image. Paramagnetic agents shorten the T_1 (spin-lattice relaxation

time), and tissues that take up a paramagnetic agent are brightened (positive enhancement). Several Gd complexes are under development or in use. Low-molecular weight GdDTPA (Gadolinium DiethyleneTriaminePentaAcetate) compounds (0.57 kDa) are used clinically for contrast enhancement of various lesions, including malignant tumors. Macromolecular contrast agents such as Gadomer-17 or albumin-GdDTPA, remain in the intravascular space with a half life of several hours because of their large molecular weights (approximately 35 or 65 kDa, respectively). Analysis of relaxivity changes induced by an intravascular agent can be used to determine blood or vascular volume and vascular permeability [18,19]. Recently, receptor-targeted contrast agents have been designed, where the contrast is derived from the density of receptor expression [20]. Of the three parameters mainly used to characterize tumor vasculature, currently, only vascular volume and vascular permeability can be quantified with contrast-enhanced proton imaging. However, quantitative blood flow measurements have been obtained using deuterium MRI with D_2O as the blood flow tracer [21].

Assessing Features of Tumor Perfusion by Dynamic ^{1}H-MRI Studies of GdDTPA Uptake

In the context of tumor therapy, it is important to know how efficiently blood is providing oxygen, nutrients and drugs to tumor tissue and how effective it is in removing waste products from that tissue. In most tumors, only 20% to 80% of the microvessels are perfused at a given time [22], which results in a considerable spatial and temporal heterogeneity of the microcirculation. Therefore, techniques that reveal the spatial and temporal heterogeneity of the tumor microcirculation will help in the development of new treatment strategies and may predict treatment outcome.

Fast dynamic ^{1}H-MRI studies of GdDTPA uptake can measure features of the *perfused* microvascular architecture with a high spatial and temporal resolution [23–25]. The regional uptake rate of this tracer into the extravascular volume of tumor tissue is related to physiological parameters that determine the supply of oxygen, nutrients and drugs, such as tumor blood perfusion (TBP) and diffusive transport across the vascular endothelium [5,26]. Different pharmacokinetic models have been developed to relate GdDTPA-uptake rates to these physiological parameters [27–29]. The most important are the single-capillary model proposed by Kety [27] or Larsson *et al.* [28] and the multi-compartment model developed by Tofts and Kermode [29]. Both models were compared in 1992 and possible differences were explained [30]. In these models, tumor tissue is considered as a volume with a vascular and extravascular compartment. The uptake of a tracer in the extravascular compartment is governed by a rate constant k (s^{-1}) and by tracer concentration differences between both compartments. The single-capillary model is more universal than the multi-compartment model, because the tracer-uptake rate constant k (s^{-1}) is related to both TBP (ml s^{-1}) and diffusive transport across the vascular endothe-

lium $(ml\ s^{-1})$, whereas in the multi-compartment model, k is only determined by diffusive transport across the vascular endothelium [29,30]. This transport term is dominated by the permeability (P) of the vascular endothelium $(cm\ s^{-1})$ and the surface-area (S) of the perfused microvessels (cm^2). Both parameters are grouped in the so-called *PS*-product, because they are difficult to measure separately. Finally, in both models, the uptake rate constant has an inverse relationship with the distribution volume (V_d) (ml) of the tracer, which is the extracellular space in the case of GdDTPA.

The choice of the pharmacokinetic model depends on the physicochemical and pharmacological properties of the tracer. For instance, diffusion-limited tracer uptake across the vascular endothelium may be favored when tracers with a molecular weight larger than 20 kDa are chosen [31] (see also Tumor Perfusion Measured with High-Molecular Weight Tracers section). In the case of small tracers, such as GdDTPA, it is more difficult to correlate tracer-uptake rates directly to TBP and/or diffusive transport across the vascular endothelium, since both may influence the tracer-uptake rate simultaneously. However, detailed information on morphometric parameters of the *perfused* neovasculature of a tumor may help to solve this problem.

In pre-clinical studies on 9L-glioma growing in rat brain, the perfused vascular surface-area (S) was determined immunohistochemically and co-registered with images of fast dynamic GdDTPA uptake [31]. Spatial matching of S with GdDTPA-uptake rates revealed a linear relationship (see Figure 1*A*). The linear relationship suggests that GdDTPA-uptake rates (k) are dominated by S and hence, are not significantly affected by variations in TBP or vascular permeability (P). The molecular weight of GdDTPA is probably not large enough to discriminate between more or less leaky microvessels, because all microvessels were highly permeable to GdDTPA. Furthermore, it would be of interest to know which range of TBP values could affect the relationship between k and S. For that purpose, relationships between k-values, *PS*-product and TBP were simulated using the single-capillary model. In these simulations, the TBP was varied between 0 and 4 times the maximum *PS*-product found in the study on 9L-glioma growing in rat brain [31]. In Figure 1*B*, it is shown that the relationship between k-values and the *PS*-product becomes linear only when the TBP is larger than the *PS*-product. Thus, the linear relationship between k-values and the perfused vascular surface area in Figure 1*A* suggest that TBP is larger than the *PS*-product in the different voxels. Hence, GdDTPA-uptake rates are *diffusion-limited*. If the TBP was less than the *PS*-product, the relationship between k and *PS*-product would be exponential, showing that GdDTPA-uptake rates were *perfusion-limited*. When GdDTPA-uptake rates can be related to parameters of the functional neovasculature, they can be used more efficiently as a prognostic tool before or during the monitoring of a therapy. For instance, this may help to monitor non-invasively the effect of an anti-angiogenic therapy on tumor microvessels.
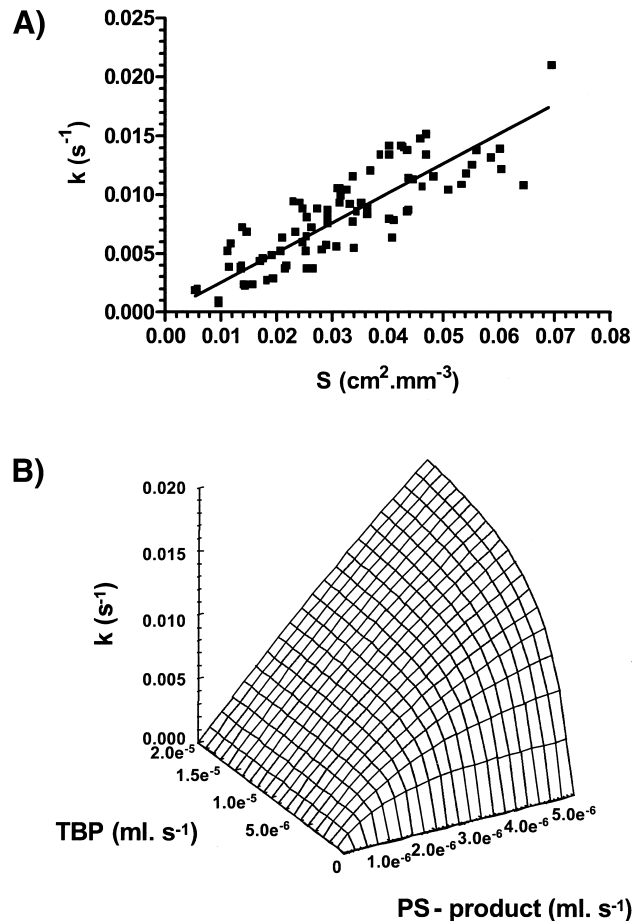

A)

B)

Figure 1. *(A) The correlation between GdDTPA-uptake rates (k) and the perfused vascular surface-areas (S) in voxels of 10 9L-gliomas. The solid line indicates the results of the least-squares linear regression analysis of the data: $k = 0.23 \pm 0.02\ SD \times S$, $R^2 = 0.72$ $(n = 86)$. (B) Surface-plot of correlations between the PS-product $(x$-axis$)$, TBP $(y$-axis$)$ and GdDTPA-uptake rate constants (k) $(z$-axis$)$ using the definition of the rate constant k as proposed by Kety [27] or Larsson et al. [28]. Note that the range of k-values is comparable to the range in (Figure 2A). These data are from work performed by B. van der Sanden with grateful acknowledgements to Dr. T.H. Rozijn, Dr. W.M.M.J. Bovee, P.F.J.W. Rijken, Prof. A.J. van der Kogel and Prof. A. Heerschap.*

Tumor Perfusion Measured with High-Molecular Weight Tracers

GdDTPA conjugated to high molecular weight tracers can be used to generate three-dimensional maps of vascular volume and permeability [32,33]. Multi-slice data obtained for a human breast cancer model (MDA-MB-435-1β) in a SCID mouse are presented in (Figure $2a - f$). At the end of the imaging studies, the animals were sacrificed, 0.5 ml of blood withdrawn from the inferior vena cava, and tumors were marked for referencing to the MRI images, excised and fixed in 10% formalin for sectioning and staining.

In the MR images, the relaxation rate $(1/T_1)$ was determined in each voxel as a function of time. The slopes of these relationships were used to compute (PS) maps (Figure 2*b*). The intercept of the line at zero time is used to compute vascular volume maps, shown in (Figure 2*c*) [34]. In this manner, vascular volumes are
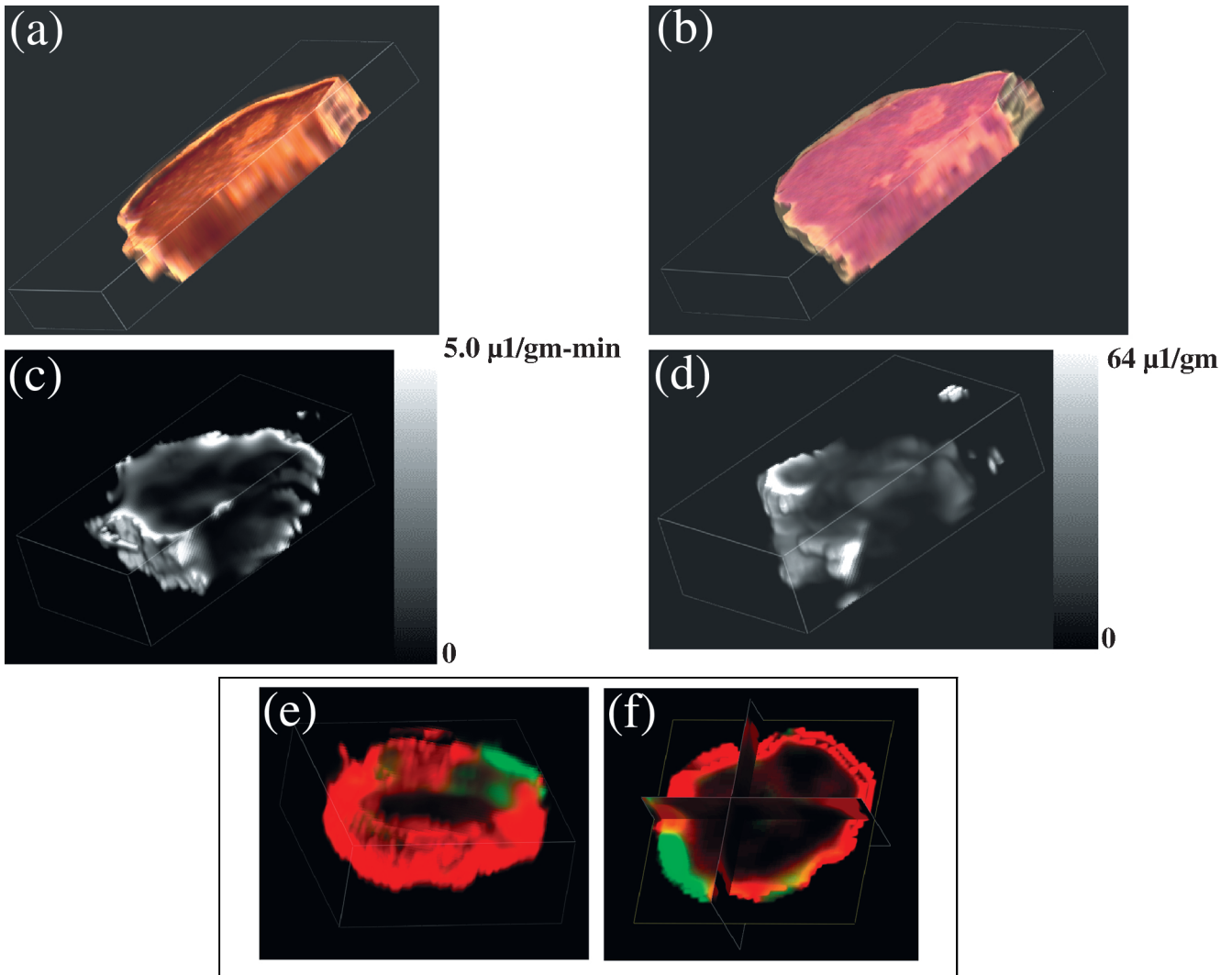
Figure 2. Three-dimensional reconstructed maps obtained from a single MDA-MB-435-1β tumor. (a) Sections stained for VEGF expression using a rabbit polyclonal anti-VEGF antibody (Santa Cruz Biotechnology, Santa Cruz, CA). (b) Hematoxylin/eosin-stained histologic sections. (c) MRI map of vascular permeability. (d) MRI map of vascular volume. (e,f) Three-dimensional and triplanar views of a fused vascular image obtained by displaying vascular volume through a green channel and vascular permeability through a red channel. Multi-slice maps of relaxation rates (T_1^{-1}) were obtained by a saturation recovery method combined with fast T_1 SNAPSHOT-FLASH imaging (flip angle of 5°, echo time of 2 msec). Images of eight slices (slice thickness of 1 mm) acquired with an in-plane spatial resolution of 250 μm (64×64 matrix, 16 mm field of view, NS = 16) were obtained for three relaxation delays (100 msec, 500 msec, and 1 second) for each of the slices. Thus, 64×64×8 T_1 maps were acquired within 7 minutes with an M_o map with a recovery delay of 7 seconds acquired once at the beginning of the experiment. Images were obtained before i.v. administration of 0.2 ml of 60 mg/ml albumin-GdDTPA in saline (dose of 500 mg/kg) and repeated every 8 minutes, starting 10 minutes after the injection, up to 32 minutes. Relaxation maps are reconstructed from data sets for three different relaxation times and the M_o data set on a pixel-by-pixel basis. These data are from work performed by D. Artemov, M. Solaiyappan and Z. M. Bhujwalla.

corrected for vessel permeability. Adjacent 5-μm-thick histologic sections obtained at 500-μm intervals through the tumor were stained with hematoxylin/eosin or for distribution of VEGF. Sections were digitized with a Sanyo CCD camera attached to an optical microscope. Three-dimensional reconstructions of both MRI and histologic sections (Figure 2a and b), were performed using the Clinical Microscope Visualization software running on Silicon Graphics Inc., Octane Workstation. Image cross-registration was performed interactively. Also shown in Figure 2e and f are the fusion of vascular volume and vascular permeability displayed as two independent colors, green and red. The absence of yellow in most of the image demonstrates visually that there is very little overlap between regions of high vascular volume and regions of high permeability. This characteristic has been consistently observed. Regions of low vascular volume often contain necrotic foci and are also the most permeable [17]. These regions are also usually associated with higher expression of VEGF. These data support earlier MRI observations made by Furman-Haran et al. [35] that highly permeable vessels were detected near necrotic regions for MCF-7 tumors. Another possibility is that tumor vessels appear leaky in these regions (especially in the clinic) because they have been destroyed by an advancing invasive tumor mass.

Ethylnitrosourea induces breast tumors fibroadenomas (FA), as well as low and high grade infiltrating ductal carcinomas (IDC) in the rat. Using this system, the pharmacokinetic characteristics of Gd-DTPA (<1 kD), Gadomer-17 (35 kD), and albumin-Gd-DTPA (70–90 kD) were evaluated by Dynamic Contrast Enhanced MRI in order to differentiate the different tumor types [18]. The benefits of using three different sized contrast agents is that a greater range in permeability values can be discriminated. The results indicated that vascular volume was a consistent determinant of tumor grade. Although high-grade IDC had the highest vascular permeability, this parameter was somewhat more variable in that FA had a higher vascular permeability than that of low-grade IDC. The statistical analyses showed that the clinically available small agents could be used to differentiate FA from the malignant tumors, but it could not differentiate between malignant tumors of low and high grades. GdDTPA was useful in discriminating FA from IDC but could not discriminate between low and high grade IDC. The intermediate sized agent, Gadomer-17, could differentiate between high-grade and low-grade IDC, but it could not discriminate low-grade IDC from the benign FA. The largest agent, albumin-Gd-DTPA, was capable of differentiating all three tumor grades, but the low signal to noise ratio (resulting in high variation) was a major technical concern.

MRI Analysis of Tumor Angiogenesis

MRI provides multiple approaches for detection of tumor angiogenesis, based on molecular, structural and physiological distinctions between normal and tumor vasculature. Tumor neovasculature is frequently highly permeable, resulting in rapid extravasation of exogenously administered contrast material into the extracellular space. Dynamic contrast enhancement and clearance curves can be used for analysis of vascular permeability, blood volume and the extracellular volume fraction (*vide supra*). Using low-molecular weight contrast material (e.g., GdDTPA), significant correlations can be found between the parameters derived from MRI and histologic analyses of microvessel densities, but not with VEGF expression [36]. With the exception of the brain, most normal capillaries are permeable to low-molecular weight compounds such as GdDTPA. However, capillary endothelial cells stimulated with the angiogenic growth factor VEGF showed enhanced extravasation of plasma proteins. MRI analysis of VEGF-induced permeability was demonstrated using albumin-GdDTPA [37]. Treatment with neutralizing anti-VEGF antibodies led to immediate and persistent inhibition of albumin-GdDTPA extravasation [37]. Permeability measured by albumin-GdDTPA correlated spatially with elevated expression of VEGF (*vide supra*).

Thus, MRI-detected hyperpermeability can be used in many cases for *in vivo* assessment of VEGF signaling. However, the large variance in vessel permeability found in normal tissues as well as in tumors, implies that hyper-permeability cannot be used as a reliable marker of neovasculature. Alternative approaches for specific evalua-

tion of angiogenesis can be found in two recent studies, in which the MRI contrast was sensitized to molecular or structural markers of angiogenesis. In the first study, specific image enhancement of tumor neovasculature has been achieved in a model of squamous cell carcinoma in rabbit using paramagnetic polymerized liposomes conjugated with anti $\alpha_v\beta_3$ antibodies [20]. In the second study, tumor neovasculature was characterized by the increased capillary diameter. Two mechanisms of water relaxivity induced by intravascular contrast material, ΔR_2 (i.e., $1/T_2$) and ΔR_2^* (i.e., $1/T_2^*$), exhibit different dependencies on the radius of the blood vessels. Thus, the ratio of relaxivities ($\Delta R_2^*/\Delta R_2$) can be used to derive maps of capillary diameter, showing excellent agreement with histology and sensitive detection of the tumor neovasculature in experimental C6 rat glioma tumors [38].

Changes in *blood volume* associated with angiogenesis can be measured using the intrinsic contrast of blood vessels arising from deoxyhemoglobin and detected by T_2^*-weighted gradient echo images [16,39]. This method has been applied to measure, for example, the kinetics of spheroid vascularization and growth for rapidly growing C6 glioma [39], the vascular instability during the dormant phase of implanted human epithelial ovarian carcinoma spheroids [40], wound-induced tumor growth [41] and the increased angiogenic activity of human epithelial ovarian carcinoma tumors in ovariectomized hyper-gonadotropic mice [42]. These studies demonstrate that the angiogenic potential of tumors is frequently dominated by local micro-environmental changes (such as hypoxia and injury) or by systemic perturbations (such as changes in the hormonal milieu), rather than by genetic selection for angiogenic phenotype. The primary signal for tumor angiogenesis in this system was attributed to stress-induced expression of VEGF as controlled by the hypoxia-inducible transcription factor, hif-1α.

In summary, assessment of environmental, molecular, genetic and pharmacological perturbations of angiogenesis requires extensive *in vivo* analytical tools. MRI can be used to non-invasively access a wide range of parameters that reflect vascular expansion and regression. The ability of MRI to obtain three-dimensional information provides large freedom in the design of the biologic model. Moreover, almost any MRI method developed in experimental models is potentially transferable to the clinical assessment of tumor angiogenesis.

MRI Tracking of Vascular Function and Maturation Using Carbogen

Regions of active angiogenesis are often connected to regions of low blood oxygenation, due to hif-1α-induced transcription of VEGF. These volumes show large signal enhancements during exposure to elevated oxygen [43]. This signal enhancement can be used for imaging vascular functionality without intravenous administration of contrast material [44]. Oxygen is usually provided as carbogen (95% O_2/5% CO_2). The CO_2 is thought to act on baroreceptors in mature vasculature and prevent hyperoxic

vasoconstriction. Maturation of vessels is a secondary process related to the recruitment of perivascular smooth muscle cells and pericytes allowing the vessels to respond to vasoactive agents. Using this approach, reduced vascular functionality was measured in hif-1α-deficient embryonic stem cell tumors [44]. MRI has been applied for detection of changes in blood flow in response to elevated CO_2, as a physiological measure of vascular maturation [45]. Since VEGF is an essential survival factor for immature neovasculature [46], its withdrawal should lead to collapse of immature, but not mature vasculature. This was tested in subcutaneous C6 tumors containing the VEGF gene under control of an inducible (tetracycline) promotor (pTET-VEGF), and revealed the ability of MRI to predict vascular susceptibility to VEGF withdrawal [45]. These results are shown in Figure 3. In these studies, inhalation was switched between 95% air/ 5% CO_2 and carbogen. Hence, CO_2 was held constant and the only variable was O_2.

Tumor Oxygenation, pH and Metabolism

Tumor oxygenation and pH are important parameters of tumor physiology that are inextricably coupled. Both low pH and low pO_2 levels negatively impact therapy and induce maturation of more transformed phenotypes [47]. These are also coupled through metabolism such that volumes with low pO_2 are expected to be more glycolytic and hence, the most acidic.

^{19}F-NMR Techniques for the Study of Tumor Oxygenation and Response to Interventions

Hypoxic cells in solid tumors are generally found in regions of poor tumor vascularization and are thought to be responsible for reducing the effectiveness of both chemo- and radiotherapy. Vascularization in neoplastic tissue can be quite heterogeneous, allowing cells to become necrotic, chronically hypoxic (diffusion limited) or acutely hypoxic (perfusion limited). Consequently, the ability to spatially resolve tumor oxygen tension in a timely fashion would allow rapid dynamic changes in local tumor oxygen values to be evaluated in response to therapeutic interventions. The ability to study and monitor tumor hypoxia would facilitate the most efficacious administration of current treatment strategies and should stimulate new developments in solid tumor therapy.

^{19}F-NMR spectroscopy and imaging of perfluorocarbon (PFC) emulsions has been used extensively to measure oxygen tension in biologic systems [48]. The favorable biocompatibility of PFCs allows intravenous injection of these compounds in large doses. Following PFC administration, the emulsion particles are cleared from the vasculature by the reticuloendothelial system (RES) of the liver and spleen as well as macrophages in abscesses and tumors. In tumors with "leaky" vasculature, PFC particles can pass through the fenestrations in the vascular wall and accumulate in the interstitial space [49]. Oxygen-sensitive ^{19}F-NMR relies on the fact that

the NMR spin-lattice relaxation rate, R_1 ($1/T_1$), of the PFC is enhanced in direct proportion to the dissolved molecular oxygen concentration and thus allows oxygen measurements to be performed in the vicinity of the sequestered PFC. Consequently, PFC spin-lattice relaxation rates measured *in vivo* are a sensitive indicator of tumor oxygen tension and provide a powerful noninvasive method for monitoring tumor hypoxia before and during treatment.

In spite of their promise as *in vivo* oxygen probes, the molecular structure of many PFCs is not conducive to high-sensitivity ^{19}F-MRI studies of tumor oxygenation. Short T_2 relaxation times, relatively long T_1 relaxation times, compensation for chemical shift artifacts and J-modulation effects can severely reduce the ^{19}F-MRI signal intensity for many PFCs [50]. Most of these technical difficulties have been mitigated through the introduction of more NMR-compatible PFCs [50,51] and the use of time-efficient MRI-data acquisition methods [51,52]. In particular, ^{19}F-echo-planar imaging (EPI) of perfluoro-15-crown-5-ether has proven to be a useful method for measuring tumor oxygenation in experimental tumor models [51].

^{19}F-NMR spectroscopy and imaging have been used extensively to monitor changes in tumor oxygenation as a function of a variety of therapeutic interventions in animal models. ^{19}F spectroscopy measurements from RIF-1 tumors in C3H mice showed a statistically significant improvement in tumor pO_2 for a nicotinamide-treated group as compared with saline-treated controls [53]. As shown in Figure 4, ^{19}F-IR-EPI of perfluoro-15-crown-5-ether can be used to map the spatial distribution of oxygen tension in RIF-1 tumors and statistically significant changes in tumor oxygenation have been measured when the breathing gas was changed from air to carbogen [51,54]. This same imaging methodology has also been used to monitor changes in tumor oxygenation following radiotherapy [55], nicotinamide administration [53,56] and chemotherapeutic treatment with 5-fluorouracil [57].

Carbogen-Induced Changes in Tumor Oxygenation and Blood Flow Monitored by Gradient-Recalled Echo (GRE) MRI

Because the oxygenation status of cells in tumors can influence the response of those tumors to therapy [58], several approaches have focused on methods for modifying tumor oxygenation and blood flow. One such approach is breathing carbogen (95% O_2/5% CO_2), to increase the amount of dissolved oxygen in the plasma to provide more oxygen at the capillary level, and hence allow diffusion of oxygen into chronically hypoxic regions. Carbogen has been shown to enhance rodent tumor radiosensitivity [59] and, in combination with nicotinamide, is currently being re-evaluated in several European clinical trials [60,61].

A non-invasive technique to assess changes in oxygenation and perfusion, and their heterogeneous distribution within an individual tumor, would be of considerable prognostic and diagnostic clinical value. ^1H-MRI methods
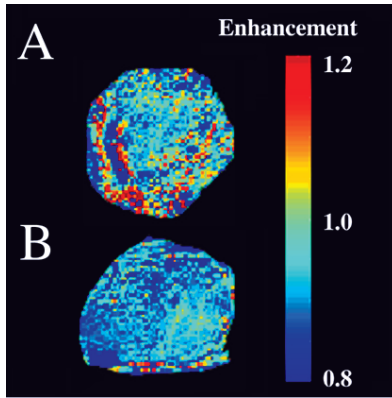
Figure 3. *Vascular collapse in response to VEGF withdrawal. Signal enhancement in response to hyperoxia was monitored in C6-pTET-VEGF tumors in nude mice, by switching the mice from inhalation of 95% air/5% CO_2 tp 95% O_2/5% CO_2 (carbogen). (A) In the absence of tetracycline, the tumors were hypervascular in accord with over-expression of VEGF. (B) Forty-eight hours after administration of tetracycline, suppressing VEGF over-expression, a significant drop in vascular function was observed (see also Refs. [20,21]). These data are from work performed by R. Abramovitch, H. Dafni, E. Smouha, L. Benjamin and M. Neeman.*

have high temporal and spatial resolution, which are sensitive to changes in deoxyhemoglobin content through the NMR relaxation time, $T_2{}^*$. Deoxyhemoglobin is paramagnetic and creates susceptibility variations in the proximity of blood vessels, shortening the MR relaxation time, $T_2{}^*$. GRE MRI sequences are sensitive to $T_2{}^*$ and hence reflect blood oxygenation levels. GRE MR images of tumors can thus be used to monitor changes in the tissue concentration of deoxyhemoglobin, whether due to fractional desaturation of oxygen from red blood cells, or blood flow modification causing changes in the absolute number of red blood cells. Deoxyhemoglobin thus acts as an endogenous contrast agent.

One of the first demonstrations of the potential of GRE MRI to the study of tumor physiology was by showing that carbogen breathing-induced large increases in image intensity of transplanted GH3 prolactinomas [62]. This increase in $T_2{}^*$ was consistent with a decrease in deoxyhemoglobin content within the tumor (Figure 5). Increases in both tumor blood oxygenation and blood flow have been discriminated within this response. Different GRE MRI responses to carbogen breathing have been observed in a number of other rodent tumor models (Ref. [62] and references therein), and the approach has also been successfully translated to the clinic, where differing GRE MRI responses of human tumors to carbogen breathing have been monitored [63]. This demonstrates that the effects are tumor-type-dependent and are presumably a consequence of different vascular architectures that exist within each tumor type.

The relationship of GRE MRI response and tumor pO_2, the critical parameter with respect to treatment outcome, has been investigated by invasive Eppendorf histography during carbogen breathing and showed a weak correlation in GH3 prolactinomas [62]. A stronger correlation of carbogen-induced increases in $T_2{}^*$ with tumor oxygen tension has
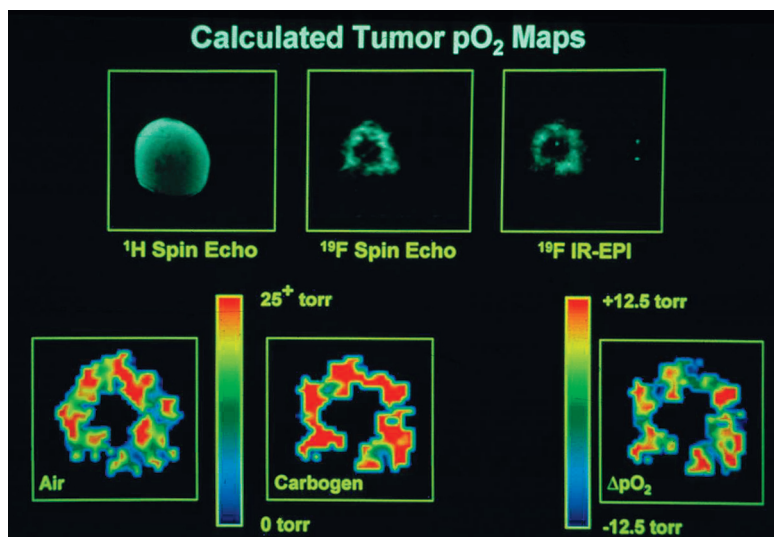

Figure 4. *Oxygen-tension mapping in a radiation-induced fibrosarcoma (RIF-1) tumor implanted on the lower back of a C3H mouse which received a 10 g/kg dose of perfluoro-15-crown-5-ether 4 days before imaging at 2.0 T. Upper Left: Coronal ^1H spin-echo image of RIF-1 tumor, 256×256 pixel resolution, repetition time (TR) = 1 second, echo time (TE) = 25 msec, field of view (FOV) = 30 mm, slice thickness of 2 mm, 128 phase-encoding steps, number of averages (NEX) = 2. Upper Center: Coronal projection ^{19}F spin-echo image of sequestered perfluoro-15-crown-5-ether in same tumor as in Upper Left, 128×128 pixel resolution, TR = 5 seconds, TE = 25 msec, FOV = 30 mm, 64 phase-encoding steps, NEX = 4, total image acquisition time = 21 minutes. Upper Right: Coronal projection ^{19}F-inversion recovery-EPI of same tumor as in Upper Left, 64×64 pixel resolution, TR = 10 seconds, TE = 30 msec, inversion time (TI) = 80 msec, FOV = 30 mm, NEX = 8, total image acquisition time = 80 seconds. Lower Left: Calculated pO_2 map (from seven IR-EPIs, like that shown in Upper Right, with TI values of 0.08, 0.20, 0.50, 1.0, 2.0, 4.0, and 8.0 seconds, respectively) for animal breathing air. Color indicates pO_2 values from 0 to >25 Torr. Lower Center: Calculated pO_2 map as in Lower Left, but with animal breathing carbogen (95% O_2/5% CO_2) for 15 minutes. Lower Right: Difference in pO_2 map obtained by subtracting pO_2 map in Lower Left from pO_2 map in Lower Center (carbogen-air). Color scale now indicates change in pO_2 from −12.5 to +12.5 Torr. Oxygen tension maps have been cropped to remove some of the background noise region shown in Upper Right. These data are from work performed by C. Sotak, with grateful acknowledgement to K. Helmer and M. Meiler.*
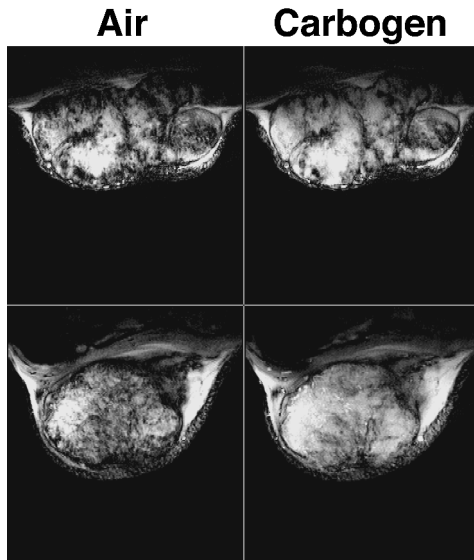
Air   Carbogen

Figure 5. *GRE images obtained from two rat transplanted GH3 prolactinomas grown subcutaneously in the flank, acquired whilst the host breathed air and subsequently carbogen (95% O_2/5% CO_2). Images are typically heterogeneous, with regions of intense signal (long T_2* hence low [deoxyhaemoglobin]) becoming more so during carbogen breathing. Within some of these regions, intensity increases can be observed for structures that are attributed to large tumor blood vessels. Other regions giving rise to little or no signal (short T_2* hence higher [deoxyhaemoglobin]) are unaffected by carbogen breathing and probably correspond to areas of either low blood flow/hypoxia or necrosis, though this has still to be addressed. These data are from work performed by S. Robinson, with grateful acknowledgement to Prof. J.R. Griffiths.*

been observed in R3230Ac mammary adenocarcinomas [64]. Preliminary data using a novel MR-compatible fiber-optic oxygen electrode have demonstrated the simultaneous acquisition of tumor GRE MR images and pO_2, and increases in both signal intensity and oxygenation status with carbogen breathing [65].

The effects of carbogen breathing on the tumor metabolic phenotype have been monitored by GRE MRI interleaved with ^{31}P-MRS, an indicator of the tumor bioenergetic state [66]. Carbogen increased both tumor GRE MR image intensity and βNTP/P_i. Host carbogen breathing did not change intracellular pH, whereas extracellular pH became more acidic (*vide infra*). Tissue and plasma glucose increased in response to carbogen, whilst intra- and extracellular lactate decreased, consistent with a switch to a more oxidative tumor metabolism.

Carbogen, in combination with nicotinamide, is being re-evaluated as a clinical radiosensitizer with some encouraging results [60,61]. However, breathing carbogen in the clinic has proven problematical, as such high levels of hypercapnia induce sensations of breathlessness and heat. In support of these trials and the development of appropriate gas mixtures for routine clinical use, both 1% and 2.5% CO_2 in oxygen were found to elicit a GRE MRI response in rat GH3 prolactinomas, the latter to a similar extent as carbogen [67]. This supports the concept that levels of hypercapnia can be reduced without loss of enhanced oxygenation and hence radiotherapeutic benefit [68].

Additionally, carbogen-induced increases in tumor blood flow have been used to enhance the uptake and efficacy of the chemotherapeutic agents ifosfamide and 5-fluorouracil, monitored by MRS [69,70]. The underlying hypothesis is that carbogen dilates the tumor blood vessels, due to CO_2-induced vasodilatation, resulting in improved drug delivery, with the resumption of air breathing closing down these vessels and trapping the drug.

The exact relationship between the GRE MRI response to carbogen and tumor blood oxygenation and flow is complicated, being a function of blood volume, blood vessel morphology, vascular density and blood flow. A similar approach is now being used to probe vascular maturation and function in tumor angiogenesis [16]. There is now a large amount of evidence suggesting that the increase in GRE MR image intensity of tumors with carbogen breathing is consistent with a decrease in deoxyhemoglobin, i.e., an improvement in tumor *blood oxygenation* (decrease in ΔT_2*). A number of issues now need to be addressed, namely: 1) What are the precise mechanisms underlying this response? 2) Are carbogen non-responding regions indicative of areas of tumor hypoxia or necrosis? 3) Does a decrease in T_2* reflect an increase in *tissue p*O_2?, and 4) Can any prognostic/diagnostic indices be identified from this response that will be ultimately useful in the clinic?

Tumor pH

Tumors have long been known to generate notable amounts of lactic acid even in the presence of oxygen [71]. This has led many to postulate that tumors are acidic. Indeed, early studies with microelectrodes appeared to confirm this hypothesis, since pH values as low as 6.2 were measured in many tumors [72]. However, ^{31}P-MRS of inorganic phosphate (P_i) in tumors measured pH values that were neutral-to-alkaline [73–75]. This apparent discrepancy was resolved when it was determined that the pH measured by MRS (pH$_{MRS}$) was actually measuring intracellular pH [76], and by extrapolation, microelectrodes were measuring the extracellular pH. Such reversal of pH gradients can negatively impact therapy, and this is discussed in more detail in the companion manuscript. Additionally, the apparent reversal of the pH gradient (with acid outside) has physiological and metabolic consequences to the tumor cells [77]. Low pH can also affect carcinogenesis itself. For example, culturing of primary diploid Syrian hamster embryo cells at pH 6.7 induces them to spontaneously transform to a tumorigenic phenotype [78,79]. This may occur because low pH is clastogenic, causing chromosomal strand breaks and rearrangements [80,81]. At a later stage of carcinogenesis, low pH also induces invasive, migratory behavior *in vitro* [82] as well as metastasis *in vivo* [83], apparently through the activation and release of proteases [84–87].

MR provides an almost ideal technology with which to monitor tumor pH, since it is non-invasive and non-destructive. Additionally, the resonant frequencies and behaviors of many compounds are pH-sensitive. The most

common pH indicator in use by MRS is that of endogenous P_i, which is sensitive primarily to the intracellular pH [88]. A number of ^{19}F-labeled pH indicators have been developed, which report both the intra- and extracellular pH values [89–91]. These are advantageous in that there are no endogenous ^{19}F signals to interfere with the measurement. A ^{31}P indicator has also been developed which is non-toxic and is confined to the extracellular space (Ref. [92], see also companion manuscript). This is advantageous in that it allows simultaneous measurements of intracellular pH and tumor bioenergetics. More recently, [1]H-labeled pH indicators based on imidazoles have been imaged in tumors to report pH "maps" of localized pH heterogeneity [93]. Methods of the future will likely be based on pH-sensitive relaxivity of contrast agents, which will allow true "pH imaging." A number of these compounds are being developed [94–97].

Perfusion and Metabolism

One of the unique contributions of MR methods is its ability to investigate the relationship between tumor blood flow, physiology and metabolism and to understand how the abnormal vasculature impacts on physiology and metabolism. One of the first attempts to relate tumor perfusion to metabolism was by Evelhoch et al. [98]. These authors observed a correlation between the well-perfused fraction (or the fraction of viable cells) and pH_{MRS} and NTP/P_i, but not between the perfusion rate in the well-perfused fraction and ^{31}P-NMR spectral parameters. They concluded the probable existence of a threshold in perfusion rate beyond which metabolism as measured by ^{31}P-NMR was not significantly coupled to perfusion. Similarly, Terpstra et al. [99] have observed a threshold for blood flow ranging from 4.8 to 20.8 ml/100 g per minute, above which lactate was constant in a C6 rat glioma model. These putative thresholds will, however, also depend on the energy requirements and oxygen and nutrient consumption rates of the cells.

Abnormal tumor vasculature manifests itself as heterogeneity in metabolism and pH. Localized proton spectra obtained from a single tumor, frequently demonstrate heterogeneity in the distribution of lactate for $2\times2\times2$ mm^3 voxels through the tumor (Ref. [100], see below). This heterogeneity of lactate distribution likely translates into a heterogeneity in pH (Ref. [93], Figure 6). The versatility of current MR techniques will allow evaluation of multi-parametric relationships, e.g., lactate, extracellular pH, vascular volume and permeability, non-invasively within a single tumor. Spectroscopy has also shown that interventions which acutely alter blood flow alter metabolism. For example, administration of the vasoactive agent hydralazine which reduces tumor blood flow resulted in a significant increase in lactate as detected by localized proton spectroscopy [100]. In contrast, single doses of radiation or chemotherapy can increase tumor blood flow. A single dose of 20 Gy, which significantly increased tumor blood flow as measured by ^{14}C iodoantipyrene [101], produced a significant increase of NTP/P_i, pH and a significant decrease in lactate [101,102] as measured by MR spectroscopy. Similar changes were observed with single doses of 5-fluorouracil [103,104]. These spectroscopic data provide evidence that although the physiological environment can regulate angiogenesis, vascularization can, in turn, regulate physiology and metabolism.

Quantitative MR Studies of Glycolysis In Vivo

Under hypoxic conditions, cells in tumors derive energy primarily from glycolysis. Even in the presence of oxygen, however, an increased capacity for glycolytic metabolism is a well-established property of neoplastic cells. Many studies of experimental tumors have provided evidence of reduced respiratory capacity and increased reliance on glycolysis for energy production. Consequently, the concentration of lactic acid in tumors is usually higher than in normal tissues. Recent human studies have revealed a positive correlation between the incidence of metastasis and the mean lactate concentration in biopsies [105,106].

In vivo lactate levels can be measured with ^{1}H-MRS [107–111]. In studies of rat C6 glioma, a positive correlation has been observed between the tumor lactate level as measured in vivo with ^{1}H-MRS and the neoplastic cell density as determined ex vivo by histopathology [112]. Several groups have also demonstrated the ability to follow glycolytic breakdown of ^{13}C-enriched glucose to lactate. ^{13}C is a special NMR-active nucleus. Because it is only 1.1% naturally abundant, its consumption and conversion in tissues can be monitored in real time with tracer kinetic analyses. These MRS measurements were performed either by direct ^{13}C detection [113–117] or by more sensitive indirect detection of internuclear ([13]C-^{1}H) coupling [109,111,112,118]. The incorporation of the ^{13}C label into glutamate, which exchanges with the TCA cycle intermediate α-ketoglutarate, has permitted detection of respiratory metabolism in some tumors [113–117]. By supplying [1-^{13}C]glucose and applying the appropriate kinetic models, dynamic MRS measurements of [4-^{13}C]glutamate have allowed determinations of TCA cycle flux in cultured glioma cells [119]. Hence, in vivo MRS can provide kinetic parameters (e.g., metabolic fluxes and rate constants) to characterize neoplastic metabolism and to potentially help predict metabolic responsiveness to treatments.

Here we show results from a study of a rat C6 glioma in which ^{1}H-MRS was used to monitor the formation of [3-^{13}C]lactate using inverse-detection as a function of time while infusing [1-^{13}C]glucose. Figure 7 shows an image of a rat brain with rectangles drawn to indicate the tissue volumes from which the ^{1}H spectra originated. The top panel on the right shows the time-course of [3-^{13}C]lactate buildup in the tumor, with an expanded view of a spectrum acquired late in the [1-^{13}C]glucose infusion period. For comparison, the lower panel shows a spectrum from predominantly normal brain, which was also acquired long after the [1-^{13}C]glucose infusion had begun. In the tumor, detectable ^{13}C enrichment was observed only in lactate, whereas the brain exhibited the expected ^{13}C-labeling of glutamate, which indicated that the label cycled through the TCA cycle. Previously, low lactate levels have been observed in tissues
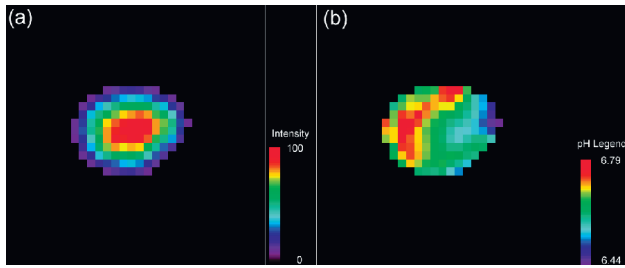
Figure 6. *(a) Intensity map of the H2 resonance of IEPA in a coronal slice through an MDA^{mb}-435 human breast cancer tumor growing in an SCID mouse. (b) Corresponding extracellular pH map, calculated from the chemical shift of the IEPA resonance (Ref. [93]) (reprinted with permission from Wiley-Liss). These data are from work performed by R. van Sluis, with grateful acknowledgement to Prof. R.J. Gillies and Dr. N. Raghunand.*

surrounding these tumors [111], and thus, the presence of [3-^{13}C]lactate in this brain region was most likely due to some inclusion of tumor tissue in the volume.

A kinetic model can be applied to calculate metabolic fluxes from dynamic MRS data like those shown above.

For C6 glioma, the rate constant describing lactate turnover was determined to be 0.043 ± 0.007 min^{-1} (mean $\pm$ SD, $n = 12$) and the average lactate efflux was 0.41 μmol/g wet weight per minute [118], which is in reasonable agreement with autoradiographic determinations of glucose utilization. In summary, *in vivo* MRS detection of wn>13C enrichment of metabolites could conceivably become a valuable tool to monitor metabolic responsiveness of tumors to therapies over time in single subjects. Such MRS measurements may also provide important clinical information regarding metabolic properties, and possibly malignancy, of lesions that are difficult to diagnose or biopsy.

Conclusions

Animal studies, in addition to providing important basic data on tumor physiology and metabolism, can also pave the way for advanced clinical applications. For example, Gd-based contrast agents are used in virtually every Radiological Center, although the use of time course data
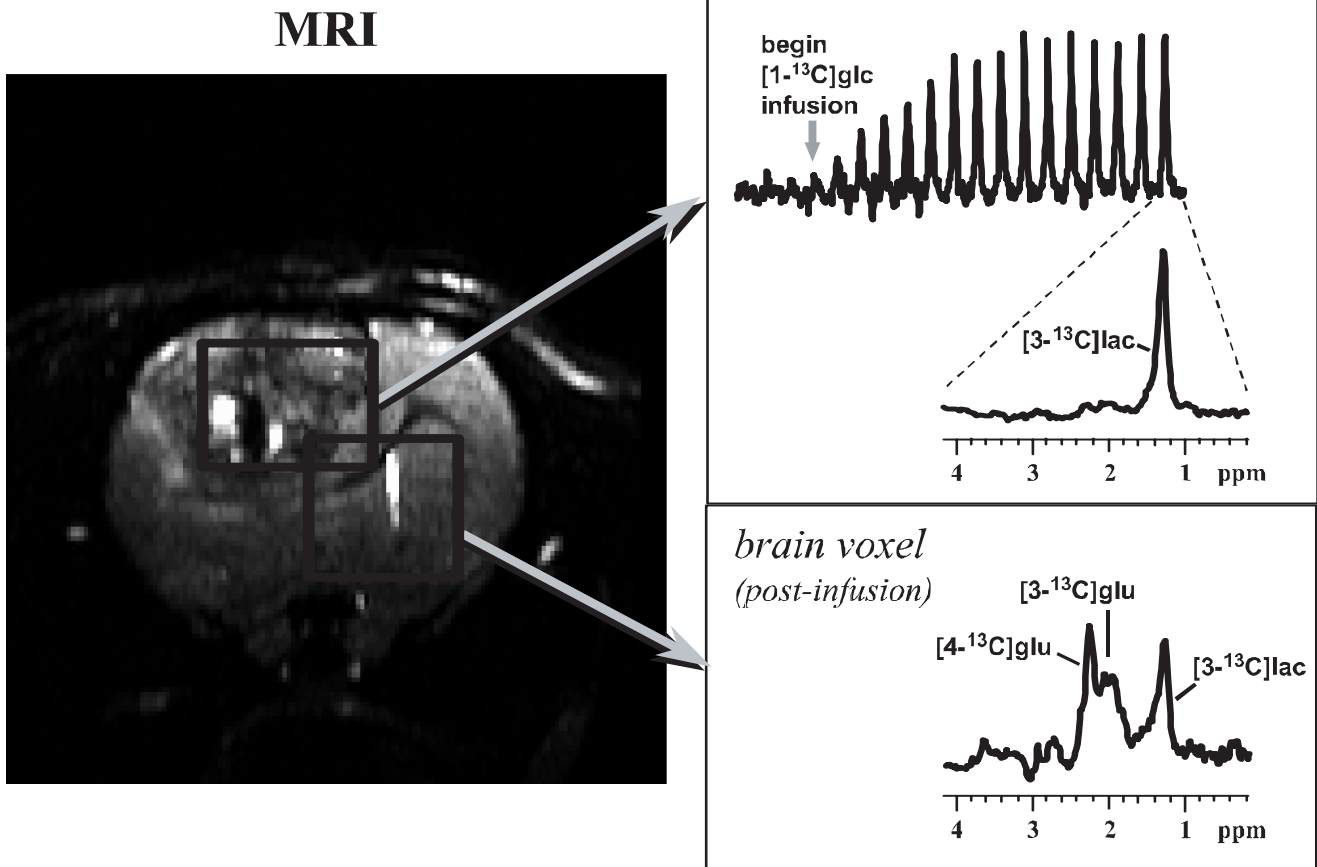

Figure 7. *The left panel shows a T_2-weighted image of a C6 glioma (coronal view). Rectangles outline two dimensions of the tissue volumes selected from tumor and the contralateral hemisphere for the spectroscopic measurements. ^{1}H spectra from tumor (b) and contralateral hemisphere (c) were acquired while infusing [1-^{13}C]glucose intravenously. These spectra were acquired with a special ^{1}H-MRS technique that detects signals from ^{13}C-labeled compounds only. These data are from work performed by M. Garwood.*

(dynamic contrast enhancement) is not as widespread. The use of higher‐molecular weight contrast agents, being developed in animals, will likely find clinical utility. BOLD experiments to assess relative deoxyhemoglobin content, can be readily applied to human tumors. Finally, even though specific indicators of physiology, such as ^{13}C glucose and indicators for pO_2 and pH, will take longer to develop, they have great clinical potential. The power of MR as a translational research tool is high, because most physical determinants of signal intensity are readily scaled from animal models to humans.

References

[1] Goldmann E (1907). The growth of malignant disease in man and the lower animals, with special reference to the vascular system. *Proc R Soc Med* **1**, 1–13.

[2] Algire GH, Chalkley HW, Legallais FY, and Park HD (1945). Vascular Reactions of normal and malignant tissues *in vivo*: I. Vascular reactions of mice to wounds and to normal and neoplastic transplants. *J Natl Cancer Inst* **6**, 73–85.

[3] Alper T, and Howard‐Flanders P (1956). Role of oxygen in modifying the radiosensitivity of *E. coli* B. *Nature* **178**, 978–979.

[4] Thomlinson RH, and Gray LH (1955). The histological structure of some human lung cancers and the possible implications for radio-therapy. *Br J Cancer* **9**, 539–549.

[5] Jain RK (1988). Determinants of tumor blood flow: a review. *Cancer Res* **48**, 2641–2658.

[6] Weidner N, Semple JP, Welch WR, and Folkman J (1991). Tumor angiogenesis and metastasis—correlation in invasive breast carci-noma. *N Engl J Med* **324**, 1–8.

[7] Horak ER, Leek R, Klenk N, LeJeune S, Smith K, Stuart N, Greenal M, Stepniewska K, and Harris AL (1992). Angiogenesis, assessed by platelet/endothelial cell adhesion molecule antibodies, as indicator of node metastases and survival in breast cancer. *Lancet* **340**, 1120–1124.

[8] Boehm T, Folkman J, Browder T, and O'Reilly MS (1997). Antiangiogenic therapy of experimental cancer does not induce drug resistance. *Nature* **390**, 404–407.

[9] Folkman J, Watson K, Ingber D, and Hanahan D (1989). Induction of angiogenesis during the transition from hyperplasia to neoplasia. *Nature* **339**, 58–61.

[10] Moses MA (1991). The Role of Vascularization in Tumor Metastasis. In: *Microcirculation in Cancer Metastasis*. F William, MR Orr Buchanan and L Weiss (Eds). CRC Press, Boca Raton, FL, pp. 257–276.

[11] Vaupel P, Kallinowski F, and Okunieff P (1989). Blood flow, oxygen and nutrient supply, and metabolic microenvironment of human tumors: a review. *Cancer Res* **49**, 6449–6465.

[12] Neufeld G, Cohen T, Gengrinovitch S, and Poltorak Z (1999). Vascular endothelial growth factor (VEGF) and its receptors. *FASEB* **13**, 9–22.

[13] Gospodarowicz D, Abraham JA, and Schilling J (1989). Isolation and characterization of a vascular endothelial cell mitogen produced by pituitary‐derived folliculo stellate cells. *Proc Natl Acad Sci* **86**, 7311–7315.

[14] Ferrara N, and Henzel WJ (1989). Pituitary follicular cells secrete a novel heparin‐ninding growth factor specific for vascular endothelial cells. *Biochem Biophys Res Commun* **161**, 851–858.

[15] Senger DR, Galli SJ, Dvorak AM, Perruzzi CA, Harvey VS, and Dvorak HF (1983). Tumor cells secrete a vascular permeability factor that promotes accumulation of ascites fluid. *Science* **219**, 983–985.

[16] Abramovitch R, Frenkiel D, and Neeman M (1998). Analysis of subcutaneous angiogenesis by gradient echo magnetic resonance imaging. *Magn Reson Med* **39**, 813–824.

[17] Bhujwalla ZM, Artemov D, and Glockner JF (1999). Tumor angiogenesis, vascularization, and contrast‐enhanced magnetic resonance imaging. *Topics in Magnetic Resonance Imaging*, 10.

[18] Su M‐Y, Wang Z, Carpenter P, Lao X, Muhler A, and Nalcioglu O (1999). Characterization of N‐ethyl‐N‐nitrosurea induced malignant and benign breast tumors in rats using three mR contrast agents. *J Magn Reson Imag* **9**, 177.

[19] Schwarzbauer C, Syha J, and Haase A (1993). Quantification of regional blood volume by rapid T1 mapping. *Magn Reson Med* **29**, 709–712.

[20] Sipkins DA, Cheresh DA, Kazemi MR, Nevin LM, Bendarski MD, and Li KCP (1998). Detection of tumor angiogenesis *in vivo* by $\alpha_v\beta_3$-targeted magnetic resonance imaging. *Nat Med* **4**, 623–626.

[21] Larcombe McDouall JB, and Evelhoch JL (1990). Deuterium nuclear magnetic resonance imaging of tracer distribution in D2O clearance measurements of tumor blood flow in mice. *Cancer Res* **50**, 363–369.

[22] Bernsen HJJA, Rijken PFJW, Oostendorp T, and Van der Kogel AJ (1995). Vascularity and perfusion of human glioma xenografted in the athymic nude mouse. *Br J Cancer* **71** (4), 721–726.

[23] Degani H, Gusis V, Weinstein D, Fields S, and Strano S (1997). Mapping pathophysiological features of breast tumors by MRI at high spatial resolution. *Nat Med* **13** (7), 780–782.

[24] Buadu LD, Murakami J, Murayama S, Hashiguchi N, Sakai S, Masuda K, Toyoshima S, Kuroki S, and Ohno S (1996). Breast lesions: correlation of contrast medium enhancement patterns on MR images with histopathologic findings and tumor angiogenesis. *Radiology* **200**, 639–649.

[25] Hulka CA, Edmister WB, Smith BL, Tan L, Sgroi DC, Campbell T, Kopans DB, and Weiskoff RM (1997). Dynamic echo‐planar imaging of the breast: experience in diagnosing breast carcinoma and correlation with tumor angiogenesis. *Radiology* **205**, 837–842.

[26] Jain RK (1987). Transport of molecules across tumor vasculature. *Cancer Metastasis Rev* **6**, 559–593.

[27] Kety SS (1951). The theory and applications of the exchange of inert gas at lungs and tissues. *Pharmacol Rev* **3**, 1–41.

[28] Larsson HBW, Stubgaard M, Frederiksen JL, Jensen M, Henriksen O, and Paulson OB (1990). Quantitation of blood‐brain barrier defect by magnetic resonance imaging and gadolinium‐DTPA in patients with multiple sclerosis and brain tumors. *Magn Reson Med* **16**, 117–131.

[29] Tofts PS, and Kermode AG (1991). Measurement of the blood‐brain barrier permeability and leakage space using dynamic mr imaging: 1. Fundamental concepts. *Magn Reson Med* **17**, 357–367.

[30] Larsson HBW, and Tofts PS (1992). Measurements of blood‐brain barrier permeability using dynamic GdDTPA scanning—a compar-ison of methods. *Magn Reson Med* **24**, 174–176.

[31] van der Sanden BPJ, Rozijn TH, Rijken PFJW, HPW Peters, Heerschap A, van der Kogel AJ, and Bovée WMMJ (1999). GdDTPA uptake rates are linearly related to the perfused microvessel density and surface‐area in 9L‐glioma growing in rat brain. *Proc Int Soc Magn Reson Med* **7**, 147.

[32] Bhujwalla ZM, Artemov D, Solaiyappan M, Mao D, and Backer JP (1999). Comparison of vascular volume and permeability for tumors derived from metastatic human breast cancer cells with and without the metastasis suppressor gene *nm23*. *Proc Int Soc Magn Reson Med* **7**, 146.

[33] Artemov D, and Bhujwalla ZM (1997). 3‐Dimensional MRI quantita-tion of tumor vascular volume and permeability. *Proc Int Soc Magn Reson Med* **5**, 491.

[34] Braunschweiger P, and Schiffer LM (1986). Effect of dexamethasone on vascular function in RIF‐1 tumors. *Cancer Res* **46**, 3299–3303.

[35] Furman‐Haran E, Margalit R, Grobgeld D, and Degani H (1996). Dynamic contrast‐enhanced magnetic resonance imaging reveals stress‐induced angiogenesis in MCF7 human breast tumors. *Proc Natl Acad Sci U S A* **93**, 6247–6251.

[36] Hawighorst H, Weikel W, Knapstein PG, Knopp MV, Zuna I, Schonberg SO, Vaupel P, and Van Kaick G (1998). Angiogenic activity of cervical carcinoma: assessment by functional magnetic resonance imaging‐based parameters and a histomorphological approach in correlation with disease outcome. *Clin Cancer Res* **4**, 2305–2312.

[37] Pham CD, Roberts TP, Van Bruggen N, Melnyk O, Mann J, Ferrara N, Cohen RL, and Brasch RC (1998). Magnetic resonance imaging detects suppression of tumor vascular permeability after administra-tion of antibody to vascular endothelial growth factor. *Cancer Invest* **16**, 225–230.

[38] Dennie J, Mandeville JB, Boxerman JL, Packard SD, Rosen BR, and Weisskoff RM (1998). NMR imaging of changes in vascular morpho-logy due to tumor angiogenesis. *Magn Reson Med* **40**, 793–799.

[39] Abramovitch R, Meir G, and Neeman M (1995). Neovascularization induced growth of implanted C6 glioma multicellular spheroids: magnetic resonance microimaging. *Cancer Res* **55**, 1956–1962.

[40] Gilead A, and Neeman M (1999). Dynamic remodeling of the vascular bed precedes tumor growth: MLS ovarian carcinoma spheroids implanted in nude mice. *Neoplasia* **1** (3), 226–230.

[41] Abramovitch R, Marikovsky M, Meir G, and Neeman M (1998). Stimulation of tumor angiogenesis by proximal wounds: spatial and temporal analysis by MRI. *Br J Cancer* **77**, 440–447.

[42] Schiffenbauer YS, Abramovitch R, Meir G, Nevo N, Holzinger M, Itin A, Keshet E, and Neeman M (1997). Loss of ovarian function promotes angiogenesis in human ovarian carcinoma. *Proc Natl Acad Sci U S A* **94**, 13203–13208.

[43] Robinson SP, Rodrigues LM, Ojugo AS, McSheehy PM, Howe FA, and Griffiths JR (1997). The response to carbogen breathing in experimental tumor models monitored by gradient-recalled echo magnetic resonance imaging. *Br J Cancer* **75**, 1000–1006.

[44] Carmeliet P, Dor Y, Herbert J-M, Fukumara O, Brusselmans K, Dewerchin M, Neeman M, Bono F, Abramovitch R, Maxwell P, Koch CJ, Ratcliffe P, Moons L, Jain RK, Collen D, and Keshet (1998). E Role of HIF-1a in hypoxia-mediated apoptosis, cell proliferation and tumor angiogenesis. *Nature* **394**, 485–490.

[45] Abramovitch R, Dafni H, Smouha E, Benjamin LE, and Neeman M (1999). *In vivo* prediction of vascular susceptibility to VEGF withdrawal: MRI of C6 rat glioma in nude mice. *Cancer Res*, **59**, 5012–5016.

[46] Benjamin LE, Golijanin D, Itin A, Pode D, and Keshet E (1998). Selective ablation of immature blood vessels in established human tumors follows vascular endothelial growth factor withdrawal. *J Clin Invest* **103**, 159–165.

[47] Gillies RJ, Schornack PA, Secomb TW, and Raghunand N (1999). Causes and effects of heterogeneous perfusion in tumors. *Neoplasia* **1** (3), 197–207.

[48] Mason RP (1994). Non–invasive physiology: ¹⁹F NMR of perfluorocarbons. *Art Cells, Blood Subs, and Immob Biotech* **22**, 1141–1153.

[49] Ratner AV, Muller HH, Simpson B-B, Johnson DE, Hurd RE, Sotak C, and Young SW (1988). Detection of tumors with 19F magnetic resonance imaging. *Invest Radiol* **23**, 361–364.

[50] Sotak CH, Hees PS, Huang H-N, Hung M-H, Krespan CG, and Raynolds S (1993). A new perfluorocarbon for use in fluorine-19 magnetic resonance imaging and spectroscopy. *Magn Reson Med* **29**, 188–195.

[51] Dardzinski BJ, and Sotak CH (1994). Rapid tissue oxygen tension mapping using 19F inversion-recovery echo-planar imaging of perfluoro-15-crown-5-ether. *Magn Reson Med* **32**, 88–97.

[52] Barker BR, Mason RP, and Peshock RM (1993). Echo planar imaging of perfluoro-carbons. *Magn Reson Imaging* **11**, 1165–1173.

[53] Hees PS, and Sotak CH (1993). Assessment of changes in murine tumor oxygenation in response to nicotinamide using 19F NMR relaxometry of a perfluorocarbon emulsion. *Magn Reson Med* **29**, 303–310.

[54] Helmer KG, Han S, and Sotak CH (1998). On the correlation between the water diffusion coefficient and oxygen tension in RIF-1 tumors. *NMR Biomed* **11**, 120–130.

[55] Dardzinski BJ, Sotak CH, Isabelle A, Murray J, and Stojadinovic P (1994). Mapping the tissue oxygen tension in RIF-1 tumors following radiation therapy using inversion recovery echo planar imaging and 19F relaxometry of perfluoro-15-crown-5-ether. *Proc Int Soc Magn Reson Med* **1**, 427.

[56] Dardzinski BJ, and Sotak CH (1994). Evaluating change in murine tumor oxygenation in response to nicotinamide by using 19F echo-planar imaging and spectroscopy. *J Magn Reson Imaging* **4**, 55.

[57] Meiler MR (1999). *In vivo* characterization of RIF-1 tumors via diffusion and Fluorine-19 NMR methods, PhD Thesis, Worcester Polytechnic Institute.

[58] Horsman MR (1998). Measurement of tumor oxygenation. *Int J Radiat Oncol Biol Phys* **42**, 701–704.

[59] Rojas A (1991). Radiosensitisation with normobaric oxygen and carbogen. *Radiother Oncol (Suppl.)* **20**, 65–70.

[60] Hoskin PJ, Saunders MI, Phillips H, Cladd H, Powell MEB, Goodchild K, Stratford MRL, and Rojas A (1997). Carbogen and nicotinamide in the treatment of bladder cancer with radical radiotherapy. *Br J Cancer* **76**, 260–263.

[61] Kaanders JHAM, Pop LAM, Marres HAM, Liefers J, Van den Hoogen FJA, Van Daal WAJ, and Van der Kogel AJ (1998). Accelerated radiotherapy with carbogen and nicotinamide (ARCON) for laryngeal cancer. *Radiother Oncol* **48**, 115–122.

[62] Robinson SP, Howe FA, Rodrigues LM, Stubbs M, and Griffiths JR (1998). Magnetic resonance imaging techniques for monitoring changes in tumor oxygenation and blood flow. *Semin Radiat Oncol* **8**, 197–207.

[63] Griffiths JR, Taylor NJ, Howe FA, Saunders MI, Robinson SP, Hoskin PJ, Powell MEB, Thoumine M, Caine LA, and Baddeley H (1997). The response of human tumors to carbogen breathing, monitored by gradient-recalled echo magnetic resonance imaging. *Int J Radiat Oncol Biol Phys* **39**, 697–701.

[64] Al-Hallaq HA, River JN, Zamora M, Oikawa H, and Karczmar GS (1998). Correlation of magnetic resonance and oxygen microelectrode measurements of carbogen-induced changes in tumor oxygenation. *Int J Radiat Oncol Biol Phys* **41**, 151–159.

[65] Maxwell RJ, Robinson SP, McIntyre DJO, Griffiths JR, Young WK, and Vojnovic B (1998). Simultaneous measurement of gradient-echo ¹H MR images and pO₂ using a fibre-optic oxygen sensor in rodent tumors and their response to carbogen breathing. *Proc Int Soc Magn Reson Med* **3**, 1665.

[66] Robinson SP, Rodrigues LM, Griffiths JR, and Stubbs M (1999). Response of hepatoma 9618a and normal liver to host carbogen (95% O₂/5% CO₂) and carbon monoxide breathing. *Neoplasia* **1** (6), 537–543.

[67] Robinson SP, Rodrigues LM, Stubbs M, and Griffiths JR (1999). Effects of different levels of hypercapnic hyperoxia on tumor GRE MR image intensity and arterial blood gases. *Proc Int Soc Magn Reson Med* **7**, 1372.

[68] Hill SA, Collingridge DR, Vojnovic B, and Chaplin DJ (1998). Tumor radiosensitization by high oxygen content gases: influence of the inspired carbon dioxide content on pO2, microcirculatory function and radiosensitivity. *Int J Radiat Oncol Biol Phys* **40**, 943–951.

[69] Rodrigues LM, Maxwell RJ, McSheehy PMJ, Pinkerton CR, Robinson SP, Stubbs M, and Griffiths JR (1997). *In vivo* detection of ifosfamide by ³¹P MRS in rat tumors: increased uptake and cytotoxicity induced by carbogen breathing in GH3 prolactinomas. *Br J Cancer* **75**, 62–68.

[70] McSheehy PMJ, Robinson SP, Ojugo ASE, Aboagye EO, Cannell MB, Leach MO, Judson IR, and Griffiths JR (1998). Carbogen breathing increases 5-fluorouracil uptake and cytotoxicity in hypoxic murine RIF-1 tumors: a magnetic resonance study *in vivo*. *Cancer Res* **58**, 1185–1194.

[71] Warburg O (1956). On the origin of cancer cells. *Science* **123**, 309–314.

[72] Wike-Hooley JL, Haveman J, and Reinhold HS (1984). The relevance of tumour pH to the treatment of malignant disease. *Radiother Oncol* **2**, 343–366.

[73] Hwang YC, Kim SG, Evelhoch JL, and Ackerman JJH (1992). Nonglycolytic acidification of murine radiation-induced fibrosarcoma 1 tumor via 3-O-methyl-d-glucose monitored by 1H, 2H, 13C, and 31P magnetic resonance spectroscopy. *Cancer Res* **52**, 1259–1266.

[74] Bhujwalla ZM, Blackband SJ, Wehrle JP, Grossman S, Eller S, and Glickson JD (1990). Metabolic heterogeneity in RIF-1 tumours detected *in vivo* by ³¹P NMR spectroscopy. *NMR Biomed* **3**, 233–238.

[75] Raghunand N, Altbach MI, Van Sluis R, Baggett B, Taylor CW, Bhujwalla ZM, and Gillies RJ (1998). Plasmalemmal pH-gradients in drug-sensitive and drug-resistant MCF-7 human breast carcinoma xenografts measured by ³¹P MR spectroscopy. *Biochem Pharmacol* **57**, 309–312.

[76] Griffiths JR (1991). Are cancer cells acidic? *Br J Cancer* **64**, 425–427.

[77] Stubbs M, Rodrigues L, Howe FA, Wang J, Jeong KS, Veech RL, and Griffiths JR (1994). Metabolic consequences of a reversed pH gradient in rat tumors. *Cancer Res* **54**, 4011–4016.

[78] LeBoeuf RA, and Kerckaert GA (1987). Enhanced morphological transformation of early passage syrian hamster embryo cells cultured in medium with a reduced bicarbonate concentration and pH. *Carcinogenesis* **8**, 689–697.

[79] LeBoeuf RA, Lin P, Kerckaert G, and Gruenstein E (1992). Intracellular acidification is associated with enhanced morphological transformation in syrian hamster embryo cells. *Cancer Res* **52**, 144–148.

[80] Morita T, Nagaki T, Fukuda I, and Okumura K (1992). Clastogenicity of low pH to various cultured mammalian cells. *Mutat Res* **268**, 297–305.

[81] Morita T, Takeda K, and Okumura K (1990). Evaluation of clastogenicity of formic acid, acetic acid, and lactic acid on cultured mammalian cells. *Mutat Res* **240**, 195–202.

[82] Martinez-Zaguilan R, Seftor EA, Seftor REB, Chu YW, Gillies RJ, and Hendrix MJC (1996). Acidic pH enhances the invasive behavior of human melanoma cells. *Clin Exp Metastasis* **14**, 176–186.

[83] Schlappack OK, Zimmermann A, and Hill RP (1991). Glucose

starvation and acidosis: effect on experimental metastasic potential, DNA content and MTX resistance of murine tumour cells. *Br J Cancer* **64**, 663–670.

[84] Montcourrier P, Silver I, Farnoud R, Bird I, and Rochefort H (1995). Breast cancer cells have a high capacity to acidify extracellular milieu by a dual mechanism. *Clin Exp Metastasis* **15**, 382–392.

[85] Rozhin J, Sameni M, Ziegler G, and Sloane BF (1994). Pericellular pH affects distribution and secretion of cathepsin B in malignant cells. *Cancer Res* **54**, 6517–6525.

[86] Cuvier C, Jang A, and Hill RP (1997). Exposure to hypoxia, glucose starvation and acidosis: effect on invasive capacity of murine tumor cells and correlation with cathepsin (L+B) secretion. *Clin Exp Metastasis* **15**, 19–25.

[87] Jang A, and Hill RP (1997). An examination of the effects of hypoxia, acidosis, and glucose starvation on the expression of metastasis-associated genes in murine tumor cells. *Clin Exp Metastasis* **15**, 469–483.

[88] Stubbs M, Bhujwalla ZM, Tozer GM, Rodrigues LM, Maxwell RJ, Morgan R, Howe FA, and Griffiths JR (1992). An assessment of 31P MRS as a method of measuring pH in rat tumors. *NMR Biomed* **5**, 351–359.

[89] Taylor JS, and Deutsch C (1983). Fluorinated-methylamino acids as 19-F NMR indicators of intracellular pH. *Biophys J* **43**, 261–267.

[90] Mason RP (1999). Transmembrane pH gradients *in vivo*: measurements using fluorinated vitamin B6 derivatives. *Curr Med Chem* **6** (6), 481–499.

[91] Aoki Y, Akagi K, Tanaka Y, Kawai J, and Takahashi M (1996). Measurement of intratumor pH by pH indicator used in 19F-magnetic resonance spectroscopy. Measurement of extracellular pH decrease caused by hyperthermia combined with hydralazine. *Invest Radiol* **31** (11), 680–689.

[92] Gillies RJ, Liu Z, and Bhujwalla ZM (1994). 31P MRS measurements of extracellular pH of tumors using 3-aminopropylphosphonate. *Am J Physiol* **267** (36), C195–C203.

[93] Van Sluis R, Bhujwalla Z, Raghunand N, Ballesteros P, Alvarez J, Cerdan S, and Gillies RJ (1999). Imaging of extracellular pH of tumors using 1H MRSI. *Magn Reson Med* **41**, 743–750.

[94] Zhang S, Wu K, and Sherry AD (1999). A novel pH-sensitive MRI contrast agent. *Angew Chem, Int Ed Engl*, in press.

[95] Ward KM, and Balaban RS (1999). Determination of pH using water proton chemical exchange: potential pH sensitive MRI contrast agents. *Proc Int Soc Magn Reson Med* **7**, 1197.

[96] Rowland IJ, Murphy PS, Schwarz A, Botta M, Aime S, and Leach MO (1998). *In vivo* extracellular pH mapping at 1.5 T using proton CSI. *Proc Int Soc Magn Reson Med* **6**, 54.

[97] Beauregard DA, Parker D, and Brindle KM (1998). Relaxation-based mapping of tumour pH. *Proc Int Soc Magn Reson Med* **6**, 53.

[98] Evelhoch JL, Sapareto SA, Nussbaum GH, and Ackerman JJH (1986). Correlation between 31P NMR spectroscopy and 15O perfusion measurements in the RIF1 murine tumor *in-vivo*. *Radiat Res* **106**, 122–131.

[99] Terpstra M, High WB, dGRA LY, Merkle H, and Garwood M (1996). Relationships among lactate concentration, blood flow and histopathologic profiles in rat C6 glioma. *NMR Biomed* **9**, 185–194.

[100] Bhujwalla ZM, Shungu DC, and Glickson JD (1996). Effects of blood flow modifiers on tumor metabolism observed *in vivo* by proton magnetic resonance spectroscopic imaging. *Magn Reson Med* **36**, 204–211.

[101] Tozer GM, Bhujwalla ZM, Griffiths JR, and Maxwell RJ (1989). Phosphorus-31 magnetic resonance spectroscopy and blood perfusion of the RIF-1 tumor following X-irradiation. *Int J Radiat Oncol Biol Phys* **16**, 155–164.

[102] Bhujwalla ZM, and Glickson JD (1996). Detection of tumor response to radiation therapy by *in vivo* proton MR spectroscopy. *Int J Radiat Oncol Biol Phys* **36** (3), 635–639.

[103] Bhujwalla ZM, McCoy CL, Glickson JD, Gillies RJ, and Stubbs M (1998). Non-invasive measurements of intra- and extracellular spaces and pH of tumors, before and after 5-fluorouracil, by 31P MR spectroscopy. *Br J Cancer* 606–611.

[104] Aboagye EO, Bhujwalla ZM, Shungu DC, and Glickson JD (1998). Detection of tumor response to chemotherapy by 1H nuclear magnetic resonance spectroscopy: effect of 5-fluorouracil on lactate levels in radiation-induced fibrosarcoma 1 tumors. *Cancer Res* **58**, 1063–1067.

[105] Schwickert G, Walenta S, Sundfor K, Rofstad EK, and Mueller-Klieser W (1995). Correlation of high lactate levels in human cervical cancer with incidence of metastasis. *Cancer Res* **55**, 4757–4759.

[106] Walenta S, Salameh A, Lyng H, Evensen JF, Mitze M, Rofstad EK, and Mueller-Klieser W (1997). Correlation of high lactate levels in head and neck tumors with incidence of metastasis. *Am J Pathol* **150**, 409–415.

[107] Hurd RE, and Freeman DM (1989). Metabolite specific proton magnetic resonance imaging. *Proc Natl Acad Sci U S A* **86**, 4402–4406.

[108] De Graaf AA, Luyten PR, Den Hollander JA, Heindel W, and Bovee WMMJ (1993). Lactate imaging of the human brain at 1.5 T using a double-quantum filter. *Magn Reson Med* **30**, 231–235.

[109] Schupp DG, Merkle H, Ellermann JM, Ke Y, and Garwood M (1993). Localized detection of glioma glycolysis using edited ^{1}H MRS. *Magn Reson Med* **30**, 18–27.

[110] He Q, Shungu DC, Van Zijl PCM, Bhujwalla ZM, and Glickson JD (1995). Single-scan *in vivo* lactate editing with complete lipid and water suppression by selective multiple-quantum-coherence transfer (Sel-MQC) with application to tumors. *J Magn Reson, Ser B* **106**, 203–211.

[111] De Graaf RA, Luo Y, Terpstra M, and Garwood M (1995). Spectral editing with adiabatic pulses. *J Magn Reson, Ser B* **109**, 184–193.

[112] Terpstra M, High WB, Luo Y, de Graaf RA, Merkle H, and Garwood M (1996). Relationships among lactate concentration, blood flow, and histopathologic profiles in rat C6 glioma. *NMR Biomed* **9**, 185–194.

[113] Ross BD, Higgins RJ, Boggan JE, Willis JA, Knittel B, and Unger SW (1988). Carbohydrate metabolism of the rat C6 glioma. An *in vivo* [13]C and *in vitro* [1]H magnetic resonance spectroscopy study. *NMR Biomed* **1**, 20–26.

[114] Lyon RC, Tschudin RG, Daly PF, and Cohen JS (1988). A versatile multinuclear probe designed for *in vivo* NMR spectroscopy: applications to subcutaneous human tumors in mice. *Magn Reson Med* **6**, 1–14.

[115] Constantinidis I, Chatham JC, Wehrle JP, and Glickson JD (1991). *In vivo* ^{13}C NMR spectroscopy of glucose metabolism of RIF-1 tumors. *Magn Reson Med* **20**, 17–26.

[116] Ronen SM, Volk A, and Mispelter J (1994). Comparative NMR study of a differentiated rat hepatoma and its dedifferentiated subclone cultured as spheroids and as implanted tumors. *NMR Biomed* **7**, 278–286.

[117] Artemov D, Bhujwalla ZM, and Glickson JD (1995). *In vivo* selective measurement of {1-[13]C}-glucose metabolism in tumors by heteronuclear cross polarization. *Magn Reson Med* **33**, 151–155.

[118] Terpstra M, Gruetter R, High WB, Mescher M, DelaBarre L, Merkle H, and Garwood M (1998). Lactate turnover in rat glioma measured by *in vivo* nuclear magnetic resonance spectroscopy. *Cancer Res* **58**, 5083–5088.

[119] Portais J-C, Schuster R, Merle M, and Canioni P (1993). Metabolic flux determination in C6 glioma cells using carbon-13 distribution upon [1-^{13}C] glucose incubation. *Eur J Biochem* **217**, 457–468.